Synthetic observations of simulated Pillars of Creation

Barbara Ercolano,[1,2]⋆ James E. Dale,[2] Matthias Gritschneder[3] and Mark Westmoquette[4]

[1]*Universitäts-Sternwarte München, Scheinerstr. 1, 81679 München, Germany*
[2]*Cluster of Excellence Origin and Structure of the Universe, Boltzmannstr. 2, 85748 Garching, Germany*
[3]*Kavli Institute for Astronomy and Astrophysics, Peking University, Yi He Yuan Lu 5, Hai Dian, 100871 Beijing, China*
[4]*European Southern Observatory, Karl-Schwarzschild-Str. 2, 85748 Garching bei München, Germany*

ABSTRACT

We present synthetic observations of star-forming interstellar medium structures obtained by hydrodynamic calculations of a turbulent box under the influence of an ionizing radiation field. The morphological appearance of the pillar-like structures in optical emission lines is found to be very similar to observations of nearby star-forming regions. We calculate line profiles as a function of position along the pillars for collisionally excited [O III] λ5007, [N II] λ6584 and [S II] λ6717, which show typical full width at half-maximum of 2–4 km s^{-1}. Spatially resolved emission-line diagnostic diagrams are also presented which show values in general agreement with observations of similar regions. The diagrams, however, also highlight significant spatial variations in the line ratios, including values that would be classically interpreted as shocked regions based on 1D photoionization calculations. These values tend to be instead the result of lines of sight intersecting which intersect for large portions of their lengths the ionized-to-neutral transition regions in the gas. We caution therefore against a straightforward application of classical diagnostic diagrams and 1D photoionization calculations to spatially resolved observations of complex 3D star-forming regions.

Key words: stars: formation – H II regions.

1 INTRODUCTION

The influence of stellar feedback on the star formation process itself is one of the most important issues in this field of astrophysics. Feedback from OB-type stars, in the form of photoionizing radiation, radiation pressure, winds and supernovae, can be both positive (i.e. enhancing or hindering the star formation efficiency) and negative and may be responsible for regulating the efficiency and rate of star formation on the scale of giant molecular clouds (GMCs).

The destructive effects of feedback, in the sense of quenching star formation, gas expulsion and dispersal of young clusters, have been studied by many authors. The dynamical influence of gas expulsion on clusters has been examined by, e.g., Hills (1980), Goodwin (1997), Boily & Kroupa (2003a,b) and Bastian & Goodwin (2006), while self-regulation of star formation by limiting the star formation efficiency has been modelled by, e.g., Whitworth (1979), Bodenheimer, Tenorio-Tagle & Yorke (1979), Tenorio-Tagle & Bodenheimer (1988), Franco, Shore & Tenorio-Tagle (1994) and Matzner (2002).

Conversely, numerous authors have studied the positive effects of feedback in the context of induced or triggered star formation, partly spurred on by a recent crop of exquisite observations of triggering apparently in progress. The popular collect-and-collapse model of triggering has been studied analytically and numerically many times (e.g. Whitworth et al. 1994; Wünsch & Palouš 2001; Dale, Bonnell & Whitworth 2007a) and has been observed in action (e.g. Zavagno et al. 2006; Deharveng et al. 2008; Zavagno et al. 2010). However, for this model to be valid, it is necessary to assume that the gas on which feedback is acting is relatively smooth and quiescent, conditions which are not always met, especially not in the inner regions of turbulent GMCs where the density and velocity fields in the gas are highly inhomogeneous. Under these conditions, it is very difficult to devise an analytic description of the effects of feedback.

This question has instead been approached numerically by means of hydrodynamical simulations modified to include the thermal effect of photoionization. The complexity of such simulations and the inevitable dependence of the results on the chosen initial conditions demand strict comparisons with observations before meaningful conclusions may be drawn. One such test for how realistic these models are involves running large-scale cluster simulations and computing statistics for (e.g.) the initial mass function (IMF)

⋆E-mail: ercolano@usm.lmu.de

of the stars and their multiplicity. Such statistics, however, are often difficult to obtain with the required accuracy. The stellar IMF is a steep function, and at least several hundred stars are required to adequately sample it over a meaningful range of masses. Combined with the difficulty of modelling feedback itself, this problem requires large and time-consuming calculations (Klessen, Krumholz & Heitsch 2009; Dale & Bonnell 2011).

Another approach is to compare the morphology of structures in the interstellar medium (ISM) that are influenced by the effects of photoionizing radiation. Spatially resolved imaging [e.g. from the *Hubble Space Telescope* (*HST*)] and spectroscopy of young star-forming regions (e.g. Hester et al. 1996; Pound, Reipurth & Bally 2003; Gahm et al. 2006; Matsuura et al. 2007; Smith, Bally & Walborn 2010; Westmoquette et al. 2010) provide a wealth of crucial information and hold the promise of helping constrain models of ISM evolution. Until now, the problem of realistically computing the observable radiation fields from systems produced by hydrodynamical calculations has only been moderately explored (Arthur et al. 2011). The main reason for this is that the majority of hydrodynamical codes only include the thermal effects of photoionization in a very approximate fashion (see Dale, Ercolano & Clarke 2007b; Ercolano & Gritschneder 2011a), preventing the calculation of the detailed thermal and ionization structure of the gas required for the prediction of emission line and continuum radiation from the region. A solution to this problem is to employ a dedicated 3D photoionization code as a post-processing step to analyse the emission from density snapshots of the hydrodynamical calculations.

We use this approach in this paper to explore the observational appearance of the star-forming pillars obtained by the recent calculations of Ercolano & Gritschneder (2011b, hereafter EG11), which modelled the impact of radiation from high-mass stars on the turbulent ISM. The calculations improved upon the previous work of Gritschneder et al. (2009b, 2010) by including the effects of diffuse ionizing radiation fields on the hydrodynamics and thus on the shaping of the ISM and the formation of pillar-like structure. EG11 found that the diffuse fields promote the detachment of dense clumps and filaments from the parent cloud, and produce denser and more spatially confined structures. In this paper, we wish to investigate the observational appearance of such structures in optical emission to verify the morphological similarity to observations and to explore the potential of spatially resolved line ratio diagnostics.

We describe our numerical methods in Section 2 and the main results in Section 3. Section 4 contains a brief summary and conclusions.

2 NUMERICAL METHODS

2.1 Hydrodynamical calculations

The hydrodynamic simulations were performed with the Tree-SPH/ionization code IVINE (Gritschneder et al. 2009a). IVINE treats the ionization of the turbulent ISM under the assumption of plane-parallel irradiation on the computational domain. The surface facing the ionizing source is decomposed into equally spaced bins, whose size is chosen according to the smoothing length of the particles there. The bins or rays are subsequently refined as the radiation penetrates the gas according to the local smoothing length. Along these rays, the optical depth is calculated and a new pressure

is assigned to each particle i according to

$$P_i = \left(\frac{T_{hot}\eta_i}{\mu_{hot}} + \frac{T_{cold}(1-\eta_i)}{\mu_{cold}} \right) \frac{k_B\rho_i}{m_p}. \tag{1}$$

Here, η is the ionization degree defined as the ratio of the number density of free electrons to the total number of hydrogen nuclei and $T_{hot} = 10^4$ K, $T_{cold} = 10$ K, $\mu_{hot} = 0.5$ and $\mu_{cold} = 1.0$ are the temperatures and the mean molecular weights of the ionized and neutral gas in the case of pure hydrogen, respectively. k_B is the Boltzmann constant, m_p is the proton mass and ρ_i is the density of the smoothed particle hydrodynamics (SPH) particle.

In the results presented here, the diffuse ionization is included according to EG11. The shadowed particles with a density lower than $n = 100$ cm^{-3} are assigned a new, higher temperature according to a fitted function. This function is derived from comparisons of previous simulations with full 3D post-processing using the MOCASSIN code (Ercolano et al. 2003; Ercolano, Barlow & Storey 2005; Ercolano et al. 2008). The cold, dense, neutral gas is kept at a temperature of $T_{cold} = 10$ K under the assumption that it can cool fast enough, i.e. it is treated as isothermal.

Hydrodynamic and gravitational forces are then calculated for the particles with the accuracy parameters given in Gritschneder et al. (2009b). The initial density and velocity distribution mimics the turbulent ISM at Mach 5 inside a computational domain of 4 pc^3 with a mean density of $n = 300$ cm^{-3}. To create synthetic observations of the resulting structures discussed in EG11, we take a subdomain starting from the irradiated surface at the $y = 0$ plane and spanning 3 pc in the y-direction and 1 pc in the x- and z-directions around the most prominent features of the simulations in EG11. We map the hydrodynamic quantities in this region on an equally spaced grid (384×128^2). With this data, we perform the post-processing with MOCASSIN described below.

2.2 Photoionization calculations

We used the 3D photoionization code MOCASSIN (Ercolano et al. 2003, 2005, 2008) to compute the detailed ionization and temperature structure from the 5-kyr snapshot of the above-described region containing the main pillar in the EG11 simulation. The code uses a Monte Carlo approach to the transfer of radiation, allowing the treatment of both the direct stellar radiation and the diffuse fields for arbitrary geometries and density distributions. The gas is heated mainly by photoionization of hydrogen and other abundant elements. Cooling is dominated by collisionally excited lines of heavy elements, but contributions from recombination lines, free–bound, free–free and two-photon continuum emissions are also included. We have assumed typical H II region abundances for the gas phase, namely (given as number densities with respect to hydrogen): He/H = 0.1, C/H = 2.2e−4, N/H = 4.0e−5, O/H = 3.3e−4, Ne/H = 5.0e−5, S/H = 9.0e−6.

Emission lines produced in each volume element are then computed by solving the statistical equilibrium problem for each atom and ion at the local temperature and ionization conditions. The atomic data base includes opacity data from Verner et al. (1993) and Verner & Yakovlev (1995), energy levels, collision strengths and transition probabilities from version 5.2 of the CHIANTI data base (Landi et al. 2006, and references therein) and the hydrogen and helium free–bound continuous emission data of Ercolano & Storey (2006).

The current version of the code can treat the atomic and ionized gas phases and dust, but no chemical network is currently included,

preventing the calculation of physical conditions and emission from photodissociation or molecular regions (but see Bisbas et al. 2011, for recent developments in this area).

2.3 Visualization tool

The 3D grids of temperature, ionization structure and emission from MOCASSIN were further post-processed by means of our newly developed, PYTHON-based suite of tools, which will shortly be made freely available to the community on the MOCASSIN website (www.3d-mocassin.net). The tools provide 2D projections of the grids along the three major axes, accounting for dust extinction along the line of sight. Velocity maps, line profiles and emission-line diagnostic diagrams, like those presented in Section 3 of this paper, are also available. The new software will be distributed with an on-line manual, where further details on the available routines will be provided.

3 RESULTS

3.1 Morphology

EG11 concluded that one of the effects of diffuse fields in the simulation of pillar formation was that the structures obtained were denser, spatially thinner and that they would eventually detach from the parent turbulent cloud. The famous *HST* images of e.g. the Pillars of Creation in the Eagle nebula show, however, structures that are apparently coherent. We constructed 2D projected intensity maps of optical emission lines from the 500-kyr snapshot of the EG11 simulations to verify that the apparent morphological constraint provided by the *HST* image of coherent pillars is still respected. Fig. 1 shows a combined false colour composite image of the EG11 pillar at $t = 500$ kyr, where red is Hα, blue is [O III] $\lambda\lambda$5007, 4959 and green is a combination of the two channels. The top and bottom panels of Fig. 2 show the same region in the individual channels, respectively, Hα and [O III] $\lambda\lambda$5007, 4959. All images account for dust extinction along the line of sight, for the length of the simulation box, according to the interstellar extinction curve of Weingartner & Draine (2001) for a Milky Way grain size distribution for RV = 3.1, with C/H = bC = 60 ppm in lognormal size distributions, but renormalized by a factor of 0.93. This grain model is considered to be appropriate for the typical diffuse H I cloud in the Milky Way.

The figure clearly shows that the line-of-sight integrals of emission lines from the ionized gas at the surface of the pillars give the desired appearance of internally coherent structures. The spatial thickness of such structure is of the order of a tenth of a parsec, which is consistent with observations.

3.2 Line profiles

The gas velocity information combined with the emission measure at each volume element allows us to compute predicted emission-line profiles along the structures. This is shown in Fig. 3 where the predicted profiles for Hα (top right), [O III] λ5007 (top left), [N II] λ6584 (bottom left) and [S II] λ6717 (bottom right) are shown. The width of each box is 30 km s^{-1} (centred on zero) and the emissivities are in arbitrary units normalized across the regions to the brightest lines. Typical full width at half-maximum (FWHM) for the profiles are 2–4 km s^{-1}. It is useful to note at this point that Westmoquette et al. (2009) report the presence of both a narrow ($\sim$20 km s^{-1}) and a broad (50–150 km s^{-1}) component in the Hα line profiles from their optical/near-infrared integral field unit (IFU) observations of a gas pillar in the Galactic H II region NGC 6357, which contains the young open star cluster Pismis 24. They interpret the broad component as being formed in ionized gas within turbulent mixing layers on the pillar's surface, generated by the shear flows of the winds from the O stars in the cluster. Our simulations do not include stellar winds and are instead influenced only by the thermal pressure of the hot ionized gas. Relative gas velocities therefore cannot exceed a few times the speed of sound in the ionized gas, approximately 10 km s^{-1}, which explains why we only can reproduce the narrow component of the emission lines.

3.3 Line ratio diagnostics

Emission-line ratios are often used as diagnostics of gas properties such as temperature and density, and sometimes also to distinguish between shock- and photo-ionization in the gas. The development of diagnostic tools dates back to more than 40 years ago when 3D photoionization models started being developed (e.g. Harrington 1968). Diagnostic diagrams were successively developed based on grids of 1D photoionization models often calibrated with empirical data from spatially unresolved observations. Some of the most widely used diagnostic diagrams are the so-called BPT diagrams (Baldwin, Phillips & Terlevich 1981), which consist of comparing
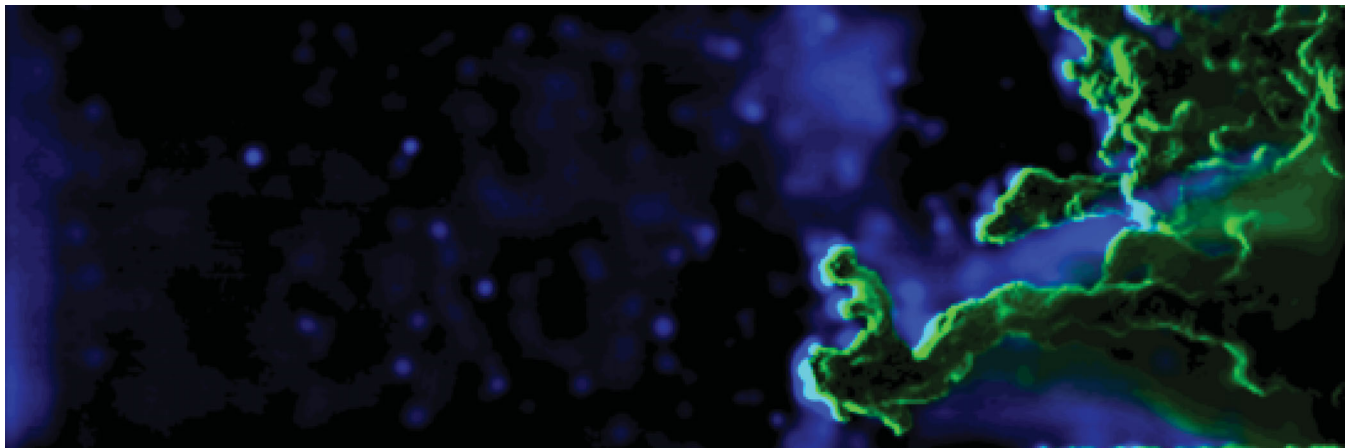

Figure 1. False colour composite image of the EG11 pillar at $t = 500$ kyr, where red is Hα, blue is [O III] $\lambda\lambda$5007, 4959 and green is a combination of the two lines.

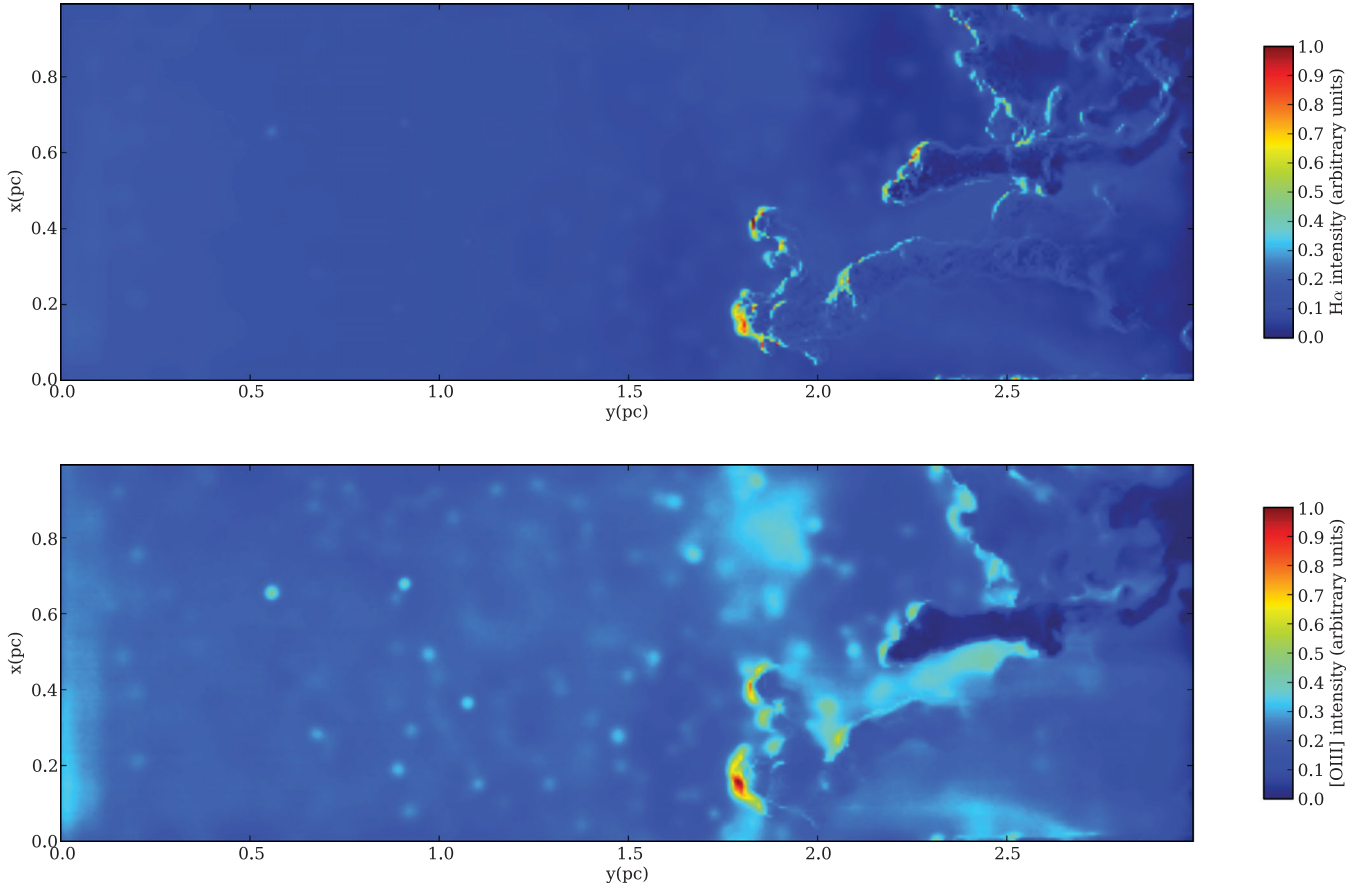**Figure 2.** Top panel: Hα image of the EG11 pillar at $t = 500$ kyr. Bottom panel: same image in [O III] λλ5007, 4959.
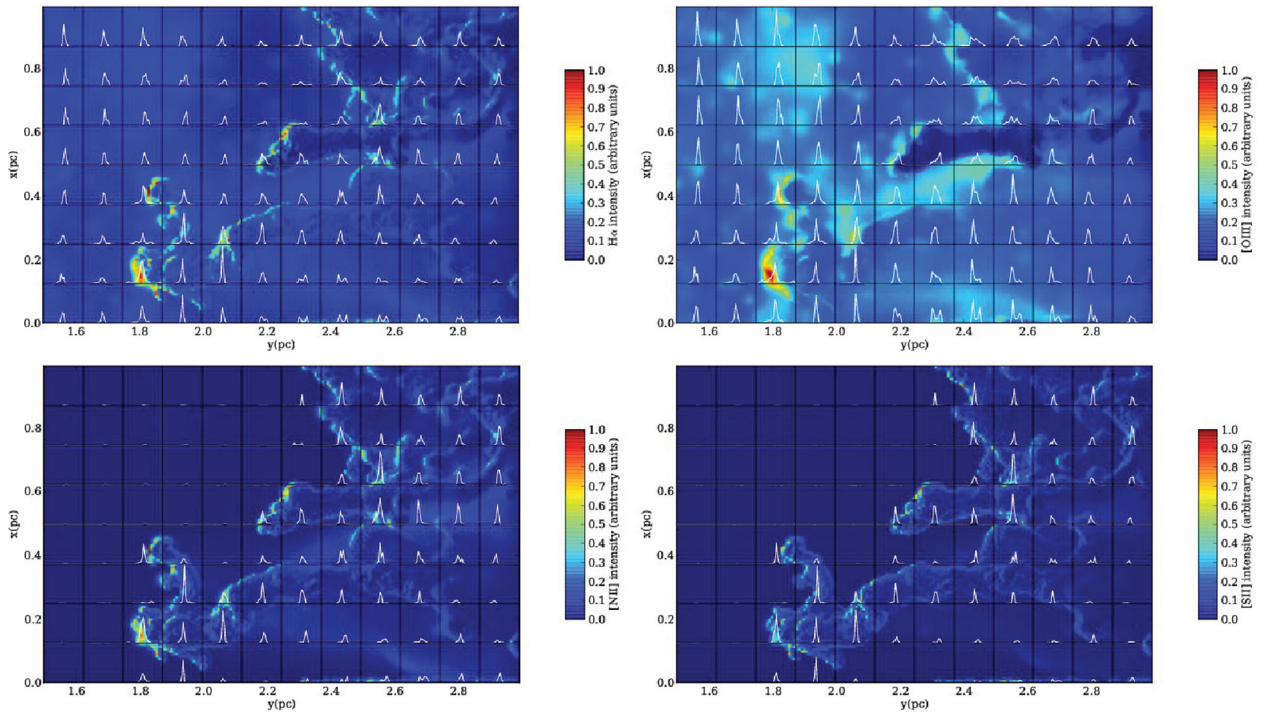

Figure 3. Predicted profiles for Hα (top right), [O III] λ5007 (top left), [N II] λ6584 (bottom left) and [S II] λ6717 (bottom right) are shown. The width of each box is 30 km s^{-1} (centred on zero) and the emissivities are in arbitrary units, normalized to the brightest line.
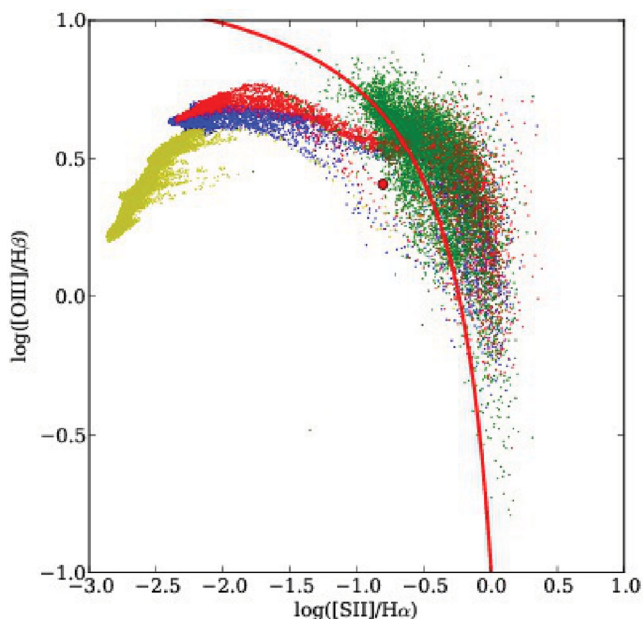
Figure 4. [O III]/Hβ versus [S II]/Hα at each pixel on the 2D projected images. The integrated value for all pixels is shown as the red point on the figures. The solid red line represents the Kewley et al. (2001) line separating star-forming galaxies from AGN. The points are colour coded according to distance from the left-hand side of the simulation box. The green points are for $y > 2.6$ pc, red for $2.6 > y > 2.2$ pc, blue for $2.2 > y > 1.8$ pc and yellow for $y < 1.8$ pc.

Figure 5. [O III]/Hβ versus [N II]/Hα at each pixel on the 2D projected images. The integrated value for all pixels is shown as the red point on the figures. The solid red line represents the Kewley et al. (2006) line separating star-forming galaxies from AGN, while the dashed line shows the line from Kauffmann et al. (2003) separating pure-star-forming galaxies from composite star-forming/AGN systems. The points are colour-coded according to distance from the left-hand side of the simulation box. The green points are for $y > 2.6$ pc, red for $2.6 > y > 2.2$ pc, blue for $2.2 > y > 1.8$ pc and yellow for $y < 1.8$ pc.

the ratios of strong collisionally excited lines (e.g. [O III] λλ5007, 4959, [N II] λ6583, 48 and [S II] λ6717, 31) to the main hydrogen recombination lines (e.g. Hβ and Hα). The excitation and ionization parameter in a given region can be determined by comparison of different ionized species or of lines with different temperature dependences. Calibration of models with observations has allowed regions in such plots where the line ratios are dominated by photoionization over shocks to be distinguished, and the determination of the nature of astronomical objects, e.g. H II regions, active galactic nuclei (AGNs), by comparison of their diagnostic spectra with model predictions (Kewley et al. 2001; Kauffmann et al. 2003; Kewley et al. 2006).

It is important to note, however, that such diagnostic tools were developed for spatially unresolved observations where the integrated emission from the whole galaxy or nebula was contained in a given emission-line ratio. More recently, the same tools have been applied for the interpretation of spatially resolved observations, e.g. IFU observations of extended H II regions (García-Benito et al. 2010; Relaño et al. 2010; Monreal-Ibero et al. 2011). This approach has to be taken with caution, given that a line-of-sight projection of a complex 3D structure, which contains fully ionized as well as neutral regions, is not directly comparable with the results from a radiation bound 1D (slab or spherically symmetric) photoionization model. Indeed a 2D projection of a 3D cloud will show pixel-to-pixel variations of the line ratios corresponding to the local gas conditions along the line of sight.

This is shown in Figs 4 and 5 where each pixel on the 2D projections of our pillars is plotted on typical BPT diagrams. The integrated value for all pixels is shown as the red point on the figures. The solid red line shown separates the area of the BPT diagrams that is traditionally considered to be occupied by H II regions dom-
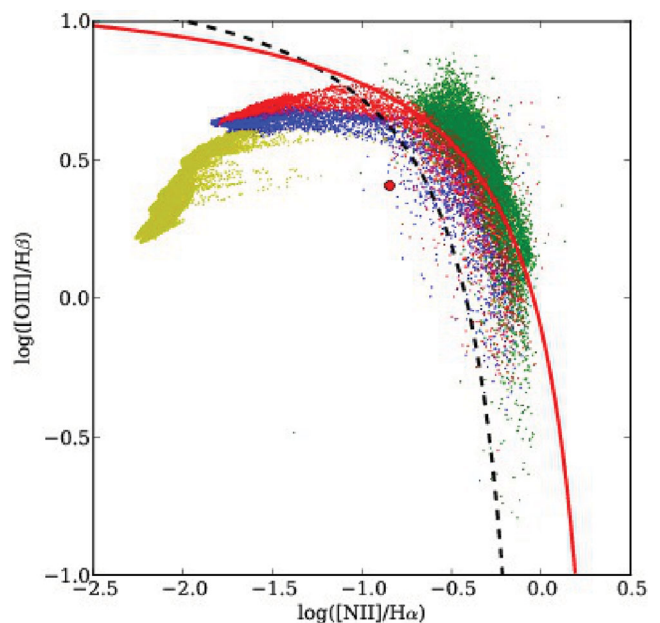
inated by photoionization (below the line) from that occupied by AGNs dominated by shock ionization (Kewley et al. 2001, 2006). The dashed line in Fig. 5 is taken from Kauffmann et al. 2003 and represents a stricter partition of the diagram in that it divides pure star-forming regions (below the line) from composite objects such as Seyfert H II galaxies whose spectra exhibit strong contributions from star formation *and* AGN. The points are colour coded by distance from the left-hand side of the simulation box on which the stellar radiation field impinges. In particular, the green points are for $y > 2.6$ pc, red for $2.6 > y > 2.2$ pc, blue for $2.2 > y > 1.8$ pc and yellow for $y < 1.8$ pc. The majority of the points lie, as expected, in the photoionization region of the diagram. However, in Fig. 4, 4 per cent and, in Fig. 5, 16 per cent of the points lie well beyond the red line, apparently suggesting that shocks may be responsible for the observed line ratios. This is of course not the case in our simulations, and the observed values are simply due to the complex 3D distribution of the gas, whereby the lines of sight at these large y-positions intersect regions of neutral or quasi-neutral gas. In the ionized-to-neutral transition regions, singly ionized N and S are relatively more abundant than in the region where hydrogen is fully ionized (the ionization potential for N^0 is 14.5 eV and that for S0 is 10.3 eV), pushing the line ratios to the right of the diagrams. The message to be taken away from these figures is that care should be taken when interpreting spatially resolved observations using diagnostic diagrams or 1D photoionization calculations, which may lead to incorrect conclusions with regard to spatial variations of abundances and/or the ionization mechanism (see also e.g. O'Dell et al. 2011 versus Wood et al., in preparation; Balick et al. 1994 versus Gonçalves et al. 2006).

4 CONCLUSIONS

We have presented synthetic observations of optical emission lines from complex density and velocity fields obtained by the 3D SPH simulations of Ercolano & Gritschneder (2011b). These calculations consist of a turbulent box irradiated by a plane-parallel ionizing field and present at 500-kyr density structures reminiscent of nearby star-forming regions (e.g. the Pillars of Creation, the Horsehead Nebula). We have performed 3D radiative transfer and photoionization calculations and produced emission-line maps in typical ionized gas tracers, including Hβ, [O III] λ5007, [N II] λ6584 and [S II] λ6717. The resulting composite three-colour images that we obtained are directly comparable with, e.g., images from the *HST* (Hester et al. 1996). The morphological appearance of our synthetic pillar images is in good agreement with the observations. We have also produced spatially resolved emission-line profiles, which show typical FWHM of 2–4 km s^{-1} and dispersions of 30 km s^{-1}, in agreement with photoionized gas with sound speeds of approximately 10 km s^{-1}.

Finally, we have studied the spatial variation of emission-line diagnostics by means of classical BPT diagrams. The volume-averaged diagnostics are consistent with the loci expected for photoionized gas; however, we show that significant location-dependent variations of the diagnostic values are to be expected, due to the complex 3D ionization, excitation and temperature distributions along the different lines of sight. In particular, we draw attention to a number of surface elements that show diagnostics consistent with gas that is shock ionized, rather than photoionized, according to the classical interpretation of the BPT diagrams by means of 1D photoionization calculations (e.g. Kewley et al. 2006). The gas in this regions, however, is not shocked, and the altered diagnostic values are only a result of lines of sight that intercept large portions of the ionized-to-neutral transition regions in the box. We therefore conclude that the straightforward application of diagnostic diagrams based on 1D photoionization calculations is not suitable to the interpretation of spatially resolved observations of complex star-forming regions.

ACKNOWLEDGMENTS

REFERENCES

Arthur S. J., Henney W. J., Mellema G., de Colle F., Vazquez-Semadeni E., 2011, MNRAS, 414, 1747
Baldwin J. A., Phillips M. M., Terlevich R., 1981, PASP, 93, 5
Balick B., Perinotto M., Maccioni A., Terzian Y., Hajian A., 1994, ApJ, 424, 800
Bastian N., Goodwin S. P., 2006, MNRAS, 369, L9
Bisbas T. G., Bell T. A., Viti S., Yates J., Barlow M., Ercolano B., 2011, in Cernicharo J., Bachiller R., eds, Proc. IAU Symp. Vol. 280, The Molecular Universe. Cambridge Univ. Press, Cambridge, p. 98
Bodenheimer P., Tenorio-Tagle G., Yorke H. W., 1979, ApJ, 233, 85
Boily C. M., Kroupa P., 2003a, MNRAS, 338, 665
Boily C. M., Kroupa P., 2003b, MNRAS, 338, 673
Dale & Bonnell, 2011, submitted
Dale J. E., Bonnell I. A., Whitworth A. P., 2007a, MNRAS, 375, 1291
Dale J. E., Ercolano B., Clarke C. J., 2007b, MNRAS, 382, 1759
Deharveng L., Lefloch B., Kurtz S., Nadeau D., Pomarès M., Caplan J., Zavagno A., 2008, A&A, 482, 585
Ercolano B., Gritschneder M., 2011a, in Alves J., Elmegreen B., Trimble V., eds, Proc. IAU Symp. Vol. 270, Computational Star Formation. Cambridge Univ. Press, Cambridge, p. 301
Ercolano B., Gritschneder M., 2011b, MNRAS, 413, 401 (EG11)
Ercolano B., Storey P. J., 2006, MNRAS, 372, 1875
Ercolano B., Barlow M. J., Storey P. J., Liu X.-W., 2003, MNRAS, 340, 1136
Ercolano B., Barlow M. J., Storey P. J., 2005, MNRAS, 362, 1038
Ercolano B., Young P. R., Drake J. J., Raymond J. C., 2008, ApJS, 175, 5345, 165
Franco J., Shore S. N., Tenorio-Tagle G., 1994, ApJ, 436, 795
Gahm G. F., Carlqvist P., Johansson L. E. B., Nikolić S., 2006, A&A, 454, 201
García-Benito R. et al., 2010, MNRAS, 408, 2234
Gonçalves D. R., Ercolano B., Carnero A., Mampaso A., Corradi R. L. M., 2006, MNRAS, 365, 1039
Goodwin S. P., 1997, MNRAS, 286, 669
Gritschneder M., Naab T., Burkert A., Walch S., Heitsch F., Wetzstein M., 2009a, MNRAS, 393, 21
Gritschneder M., Naab T., Walch S., Burkert A., Heitsch F., 2009b, ApJ, 694, L26
Gritschneder M., Burkert A., Naab T., Walch S., 2010, ApJ, 723, 971
Harrington J. P., 1968, ApJ, 152, 943
Hester J. J. et al., 1996, AJ, 111, 2349
Hills J. G., 1980, ApJ, 235, 986
Kauffman G. et al., 2003, MNRAS, 346, 1055
Kewley L. J., Dopita M. A., Sutherland R. S., Heisler C. A., Trevena J., 2001, ApJ, 556, 121
Kewley L. J., Groves B., Kauffmann G., Heckman T., 2006, MNRAS, 372, 961
Klessen R. S., Krumholz M. R., Heitsch F., 2009, preprint (arXiv:0906.4452)
Landi E., Del Zanna G., Young P. R., Dere K. P., Mason H. E., Landini M., 2006, ApJS, 162, 261
Matsuura M. et al., 2007, MNRAS, 382, 1447
Matzner C. D., 2002, ApJ, 566, 302
Monreal-Ibero A., Relaño M., Kehrig C., Pérez-Montero E., Vílchez J. M., Kelz A., Roth M. M., Streicher O., 2011, MNRAS, 413, 2242
O'Dell C. R., Ferland G. J., Porter R. L., van Hoof P. A. M., 2011, ApJ, 733, 9
Pound M. W., Reipurth B., Bally J., 2003, AJ, 125, 2108
Relaño M., Monreal-Ibero A., Vílchez J. M., Kennicutt R. C., 2010, MNRAS, 402, 1635
Smith N., Bally J., Walborn N. R., 2010, MNRAS, 405, 1153
Tenorio-Tagle G., Bodenheimer P., 1988, ARA&A, 26, 145
Verner D. A., Yakovlev D. G., 1995, A&AS, 109, 125
Verner D. A., Yakovlev D. G., Band I. M., Trzhaskovskaya M. B., 1993, Atomic Data Nuclear Data Tables, 55, 233
Weingartner J. C., Draine B. T., 2001, ApJ, 548, 296
Westmoquette M. S. et al., 2009, ApJ, 706, 1571
Westmoquette M. S., Slavin J. D., Smith L. J., Gallagher J. S., III, 2010, MNRAS, 402, 152
Whitworth A., 1979, MNRAS, 186, 59
Whitworth A. P., Bhattal A. S., Chapman S. J., Disney M. J., Turner J. A., 1994, A&A, 290, 421
Wünsch R., Palouš J., 2001, A&A, 374, 746
Zavagno A., Deharveng L., Comerón F., Brand J., Massi F., Caplan J., Russeil D., 2006, A&A, 446, 171
Zavagno A. et al., 2010, A&A, 518, L81

This paper has been typeset from a TeX/LaTeX file prepared by the author.